POLITECNICO
MILANO 1863

SCUOLA DI INGEGNERIA INDUSTRIALE
E DELL'INFORMAZIONE

Layout analysis and flight control of airships with distributed thrust

Tesi di Laurea Magistrale in
Automation and control Engineering

Filippo Cassera, 968766

Abstract: Airships, once pioneering technology nearly a century ago, are experiencing renewed research interest due to their remarkable capacity for extended flight with minimal fuel consumption. This thesis focuses into new propulsion and control technologies. Airship control has always been challenging. In order to increase controllability technological solutions such as bow thrusters and thrust vectoring have been explored, which unfortunately greatly increase the weights and complexity of construction. In light of the growing interest in high-altitude airships (HAA) and autonomous flight, one important goal is to simplify designs while maintaining performance.

This research explores control of airships using non-tilting thrusters, with a specific focus on different configurations of electro-dynamic (EHD) thrusters employed for control purposes. EHD motor utilize electrostatic forces to generate thrust through ion acceleration. If proven effective, such configurations could reduce reliance on control surfaces, tilting motors, and their associated actuators.

The primary objective of this master's thesis is to analyze how these thrusters can be strategically positioned to optimize disturbance rejection. The study aims to develop an analytical tool for comparing different motor layouts in terms of dynamic control, evaluating the effects of motor placement and quantity. The research methodology involves deriving a dynamic model from existing literature and modifying it to incorporate input from ion motors' belts. Validation of the linearized model is achieved through an eigenvalue analysis, comparing the results with existing literature. A multivariable LQR control strategy is developed to address disturbances across various configurations. Numerical simulations assess each layout's ability to restore perturbed states to equilibrium, with a defined benchmark used to evaluate performance.

The study concludes by presenting comprehensive results from numerical tests, offering insights into the influence of design parameters on performance and discussing the characteristics of an optimal layout.

Advisor:
Prof. Carlo E. D. Riboldi

Academic year:
2022-2023

Key-words: Airship, LTA, Modeling, Thrust based control, LQR, Distributed thrust, Ion thrusters

1. Introduction

Airships, also known as Lighter Than Air (LTA) vehicles, have evolved significantly since their emergence in the early 20th century, primarily in military contexts [20]. However, their popularity waned following World War II, partly due some notable accidents like the Hindenburg disaster in New York, but mainly because of the rise of high-speed aircraft and rotorcraft with greater payload capacities further limited airship proliferation.

In recent decades, there has been a renewed interest in airships, driven by their remarkable capability to remain airborne for extended durations with minimal fuel consumption. Research has explored various aspects of airship design, including their shapes, materials, and propulsion options. LTAs offer unique solutions for extended endurance missions and fuel efficiency as they rely on lifting gas expansion for buoyancy. Their versatility is further augmented by the capacity for hovering and executing vertical take-offs and landings. Small unmanned airships are finding applications in surveillance, monitoring, and meteorology.

Nevertheless, airship control has posed enduring challenges. Conventional solutions like bow thrusters and thrust vectoring have been explored to enhance maneuverability, albeit at the expense of increased weight and complexity. With growing interest in high-altitude airships (HAA) and autonomous flight, the imperative is to simplify designs while maintaining performance.

This thesis explores the application of non-tilting thrusters, specifically electro-dynamic (EHD) thrusters. Although ion thrusters provide relatively modest thrust in contrast to conventional engines, their exceptional propulsive efficiency has made them viable for space propulsion, as demonstrated in the Tianhe module of the Chinese space station. Recent advancements, such as the successful flight of a small ion-powered aircraft by a team at MIT, prove that it is possible to implement them as thrust solutions for small LTAs.

This master's thesis aims to comprehensively analyze the strategic placement of ion thrusters to optimize disturbance rejection. The study seeks to develop an analytical tool for comparing motor layouts in terms of dynamic control while assessing the impact of motor positioning and quantity.

Figure 1.1: A modern airship, Zeppelin NT D-LZZF in 2010

2. Dynamic Model of the airship

2.1. Six Degree of Freedom equations of motion

In this thesis, the prevalent mathematical model employed in airship literature is adopted. The equations governing the airship's motion are formulated using Newton's laws of mechanics. The model differs from the one normally used for aircraft [14] because the equation are written with respect to the center of buoyancy (CB) instead of the center of mass (CG). [4, 8, 13]. The body reference frame $(\cdot)_{\mathcal{B}}$ is selected, aligning the first axis with the airship's nose, second axis with the right side, and the the third axis with the bottom, as shown in Figure 2.1.

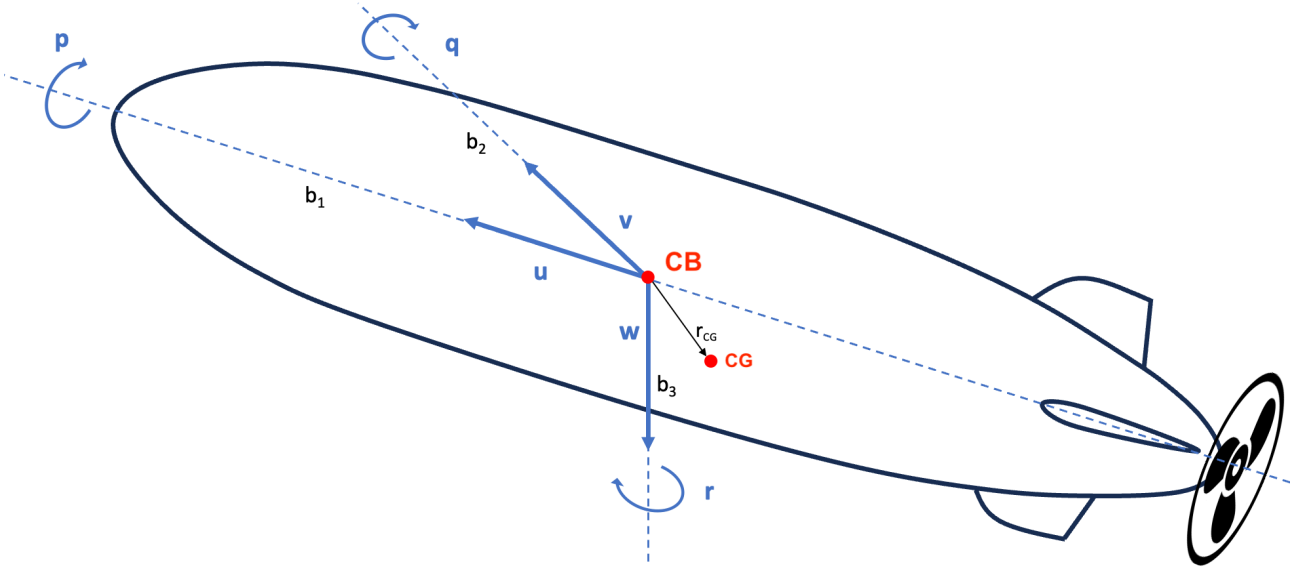

Figure 2.1: Body reference frame and Velocity components.

This model operates under the premise that the aircraft is considered a rigid body with six degrees of freedom, subjected to aerodynamic, thrust and gravitational forces. The 6-degree of freedom equations of motions for a rigid airship are:

$$\begin{bmatrix} m\boldsymbol{I}_{3\times3} & -m\boldsymbol{r}_{CG}^{\times} \\ m\boldsymbol{r}_{CG}^{\times} & \boldsymbol{J} \end{bmatrix} \begin{bmatrix} \dot{\boldsymbol{V}} \\ \dot{\boldsymbol{\omega}} \end{bmatrix} = \begin{bmatrix} -m\boldsymbol{\omega} \times (\boldsymbol{V} + \boldsymbol{\omega} \times \boldsymbol{r}_{CG}) \\ -\boldsymbol{\omega} \times (\boldsymbol{J}\boldsymbol{\omega}) - m\boldsymbol{r}_{CG} \times (\boldsymbol{\omega} \times \boldsymbol{V}) \end{bmatrix} + \begin{bmatrix} \boldsymbol{F}^{\Sigma} \\ \boldsymbol{Q}^{\Sigma} \end{bmatrix} \tag{2.1}$$

where $\mathbf{m}$ is the mass of the airship; $\mathbf{J}$ is the tensor of moments of inertia calculated with respect to CG; $\boldsymbol{r}_{CG}^{\times}$ is the skew-symmetric matrix that represents the position of CG with respect to CB ($\boldsymbol{r}_{CG}$); $\mathbf{V}$ and $\boldsymbol{\omega}$ are the linear and angular velocity expressed in body frame coordinates; $\boldsymbol{F}^{\Sigma}$ and $\boldsymbol{Q}^{\Sigma}$ represent the external loads acting on the airship.

The aircraft orientation is represented with Euler's Angles $\boldsymbol{\phi}$, $\boldsymbol{\theta}$ and $\boldsymbol{\psi}$, physically interpreted as angles of roll, pitch, and yaw. Rotational matrixis $\boldsymbol{R}_{\mathcal{I}\rightarrow\mathcal{B}}$ and $\boldsymbol{R}_{\mathcal{B}\rightarrow\mathcal{I}}$ can be used to transform a vector from inertial reference frame (earth fixed) $(\cdot)_{\mathcal{I}}$ to body fixed reference frame $(\cdot)_{\mathcal{B}}$ and vice versa. Kinematic relationships relates these angles to the angular velocities of the aircraft. [15]

2.2. External forces and moments

The forces and moments acting on the airship can be categorized into four main components: aerodynamics, gravity, buoyancy, and thrust (Equation (2.2)).

$$\begin{aligned} \boldsymbol{F}^{\Sigma} &= \boldsymbol{F}^{A} + \boldsymbol{F}^{G} + \boldsymbol{F}^{B} + \boldsymbol{F}^{T} \\ \boldsymbol{Q}^{\Sigma} &= \boldsymbol{Q}^{A} + \boldsymbol{Q}^{G} + \boldsymbol{Q}^{B} + \boldsymbol{Q}^{T} \end{aligned} \tag{2.2}$$

2.2.1 Aerodynamics

The adopted aerodynamic model in this thesis, initially developed by Kämpf [7] and later refined by Kornienko [6], distinguishes between contributions from steady and unsteady motion. Steady motion term (proportional to linear and angular velocity V, ω) corresponds to the active term commonly seen in winged flying vehicles. The unsteady term (proportional to $\dot{\omega}, \dot{V}$) is a reaction term representing the effect of added mass: the inertia added to the system due to the displacement of surrounding air by the action of the hull.

In the body frame $\mathcal{B}$, the active term can be expressed using standard aircraft dynamics notation [15]. Each component's dependence is modeled with a first-order expansion relative to kinematic variables. By considering the mutual balance of coefficients in airships with standard hull and tail configurations and proportions, the active term is:

$$\begin{bmatrix} \boldsymbol{F}_{\mathcal{B}}^{Ast} \\ \\ \boldsymbol{Q}_{\mathcal{B}}^{Ast} \end{bmatrix} = \begin{Bmatrix} X \\ Y \\ Z \\ L_{CB} \\ M_{CB} \\ N_{CB} \end{Bmatrix} = \begin{bmatrix} X_U & 0 & X_W & 0 & X_q & 0 \\ 0 & Y_V & 0 & Y_p & 0 & Y_r \\ Z_U & 0 & Z_W & 0 & Z_q & 0 \\ 0 & L_{CB_V} & 0 & L_{CB_p} & 0 & L_{CB_r} \\ M_{CB_U} & 0 & M_{CB_W} & 0 & M_{CB_q} & 0 \\ 0 & N_{CB_V} & 0 & N_{CB_p} & 0 & N_{CB_r} \end{bmatrix} \begin{Bmatrix} U \\ V \\ W \\ p \\ q \\ r \end{Bmatrix} + \boldsymbol{V}\boldsymbol{u} \tag{2.3}$$

Coefficients in the matrix of Equation (2.3) are modeled using Munk-Jones-DeLaurier theory [6, 7, 18], combining potential flow for the hull and standard incompressible lifting surface aerodynamics for the empennages [15]. Modeling depends on the hull and fins' geometry. Analytical descriptions are usually possible, especially for axis-symmetric envelopes.

In Equation (2.3), $\boldsymbol{V}\boldsymbol{u}$ represents the effects of aerodynamic surfaces that can be deflected. In this study, which employs a thrust-based control approach, this term is not considered.

The aerodynamic forcing term for the reaction component, can be characterized using Munk's shape-specific coefficients (k_1, k_2, k_3, and k'), and it is proportional to the rate of change of the generalized velocity [7]. Specifically, for axis-symmetric bodies, this term takes the following form:

$$\begin{bmatrix} \boldsymbol{F}_{\mathcal{B}}^{Aun}(\dot{\boldsymbol{\omega}}, \dot{\boldsymbol{V}}) \\ \boldsymbol{Q}_{\mathcal{B}}^{Aun}(\dot{\boldsymbol{\omega}}, \dot{\boldsymbol{V}}) \end{bmatrix} = \begin{bmatrix} \boldsymbol{F}_{11} & \boldsymbol{F}_{12} \\ \boldsymbol{F}_{21} & \boldsymbol{F}_{22} \end{bmatrix} \begin{bmatrix} \dot{\boldsymbol{V}} \\ \dot{\boldsymbol{\omega}} \end{bmatrix} \tag{2.4}$$

with

$$\boldsymbol{F}_{11} = -\rho\mathcal{V} \begin{bmatrix} k_1 & 0 & 0 \\ 0 & k_2 & 0 \\ 0 & 0 & k_2 \end{bmatrix}, \quad \boldsymbol{F}_{22} = -\rho\mathcal{V} \begin{bmatrix} 0 & 0 & 0 \\ 0 & k' J_{CB_{yy}} & 0 \\ 0 & 0 & k' J_{CB_{zz}} \end{bmatrix} \tag{2.5}$$

$$\boldsymbol{F}_{12} = \boldsymbol{F}_{12} = \boldsymbol{0}_{3\times 3}$$

where ρ is the air density, $\mathcal{V}$ the airship volume, $J_{CB_{yy}}$ and $J_{CB_{yy}}$ are the diagonal components of $\boldsymbol{J}_{CB}$, expressed in the body reference CB.

2.2.2 Gravity

Weight acts on the center of gravity, being g the gravity acceleration constant, the expression for the gravity force in the inertial reference frame $\mathcal{I}$ is:

$$\boldsymbol{F}_{\mathcal{I}}^{G} = \begin{bmatrix} 0 \\ 0 \\ mg \end{bmatrix} \tag{2.6}$$

To transform the vector from the inertial reference frame to the body-fixed reference frame $\mathcal{B}$ the rotation tensor $\boldsymbol{R}_{\boldsymbol{\mathcal{I}\rightarrow\mathcal{B}}}$ is used.

$$\boldsymbol{F}_{\mathcal{B}}^{G} = \boldsymbol{R}_{\mathcal{I}\rightarrow\mathcal{B}}\boldsymbol{F}_{\mathcal{I}}^{G} \tag{2.7}$$

Gravity force, acting at the center of gravity, also generate a moment around CB. This moment can be computed as:

$$\boldsymbol{Q}_{\mathcal{B}}^{G} = \boldsymbol{r}_{CG} \times \boldsymbol{F}_{\mathcal{B}}^{G} \tag{2.8}$$

2.2.3 Buoyancy

Similar to gravity forces, buoyancy is initially defined in the Earth-fixed frame $\mathcal{I}$, where it has a single non-null component directed upward from the ground, and then transformed into the body frame $\mathcal{B}$ using the rotational tensor. Given ρ as the air density and $\mathcal{V}$ as the volume displaced by the airship, the expression for buoyancy can be written as:

$$\boldsymbol{F}_{\mathcal{B}}^{B} = \boldsymbol{R}_{\mathcal{I}\rightarrow\mathcal{B}}\boldsymbol{F}_{\mathcal{I}}^{B} = \boldsymbol{R}_{\mathcal{I}\rightarrow\mathcal{B}} \begin{bmatrix} 0 \\ 0 \\ -\rho g \mathcal{V} \end{bmatrix} \tag{2.9}$$

Since buoyancy acts in the center of buoyancy, which is the center of body-fixed reference frame $\mathcal{B}$, it does not create any moment $\boldsymbol{Q}_{\mathcal{B}}^{B} = 0$.

2.2.4 Thrust

In common airships the thrust is generated by a rear central engine aligned with $\mathrm{b}_{1\mathcal{B}}$ axis, while control surfaces are used for directional control.

This thesis aims to delve into the use of engines for both airship control and propulsion. Each thruster's orientation is described with respect to the body reference through a swing angle σ_i and a tilt angle λ_i, according to Figure 2.2.

The contribution of every single thruster i can be computed as:

$$\boldsymbol{F}_{i\,\mathcal{B}}^{T} = \begin{bmatrix} \cos\sigma_i \cos\lambda_i \\ \sin\sigma_i \\ \cos\sigma_i \sin\lambda_i \end{bmatrix} T_i \tag{2.10}$$

where T_i is the thruster force. Being $\boldsymbol{r}_{\boldsymbol{P_{Ti}}}$ the position of the center of thrust with respect to reference $\mathcal{B}$

$$\boldsymbol{Q}_{i\,\mathcal{B}}^{T} = \boldsymbol{r}_{P_{Ti}} \times \boldsymbol{F}_{i\,\mathcal{B}}^{T} \tag{2.11}$$

The total thrust force and moment around CB are determined by summing the contributions from all thrusters N_t.

$$\boldsymbol{F}_{\mathcal{B}}^{T} = \sum_{i=1}^{N_t} \boldsymbol{F}_{i\,\mathcal{B}}^{T}, \qquad \boldsymbol{Q}_{\mathcal{B}}^{T} = \sum_{i=1}^{N_t} \boldsymbol{Q}_{i\,\mathcal{B}}^{T} \tag{2.12}$$

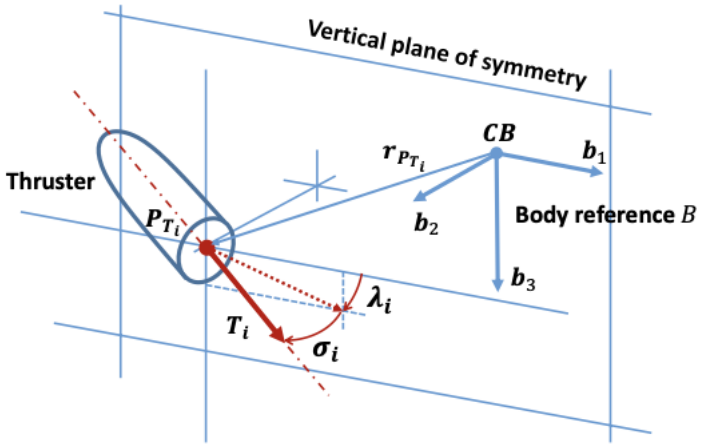

Figure 2.2: Definition of thruster position and orientation angles with respect to body reference. Swing angle σ and tilt angle λ are positive as shown with respect to reference $\mathcal{B}$ [17]

.

2.3. Complete model

By substituting external force components into Equation (2.1) and moving aerodynamic unsteady terms to the left-hand side, the model can be reformulated as follows:

$$\begin{bmatrix} m\boldsymbol{I} + \rho\boldsymbol{F}_{11} & -m\boldsymbol{r}_{CG}^{\times} \\ m\boldsymbol{r}_{CG}^{\times} & \boldsymbol{J} + \rho\boldsymbol{F}_{22} \end{bmatrix} \begin{bmatrix} \dot{\boldsymbol{V}} \\ \dot{\boldsymbol{\omega}} \end{bmatrix} = \begin{bmatrix} -m\boldsymbol{\omega} \times (\boldsymbol{V} + \omega \times \boldsymbol{r}_{CG}) \\ -\boldsymbol{\omega} \times (\boldsymbol{J}\boldsymbol{\omega}) - m\boldsymbol{r}_{CG} \times (\boldsymbol{\omega} \times \boldsymbol{V}) \end{bmatrix} + \begin{bmatrix} \boldsymbol{F}_{st}^{A} + \boldsymbol{F}^{G} + \boldsymbol{F}^{B} + \boldsymbol{F}^{T} \\ \boldsymbol{Q}_{st}^{A} + \boldsymbol{Q}^{G} + \boldsymbol{Q}^{B} + \boldsymbol{Q}^{T} \end{bmatrix} \tag{2.13}$$

2.4. Linearized model

The airship's nonlinear model is linearized using the small disturbance theory hypothesis [3].

In order to derive a linear model the following simplifying assumptions are made:

- The flight condition is steady, rectilinear, and symmetric, resulting in null rotation, linear accelerations, rotational and lateral velocity;
- The altitude remains constant and no change in the volume of the ballonets is made (so the mass and center of mass doesn't change);
- The atmosphere is assumed to be steady.

Similar to traditional aircraft, this approach allows us to derive decoupled equations for longitudinal and lateral dynamics.

For the sake of brevity in the remainder of this thesis, when discussing linearized models, we will omit the perturbation symbol (δ) for state variables but retain it for input controls.

2.4.1 Longitudinal dynamics

The longitudinal dynamic equation describe the aircraft's motion within the vertical $XZ_{\mathcal{B}}$ plane. The state vector is composed by axial and vertical velocity components, pitch rate and pitch angle $\boldsymbol{x}_{lon} = [U, W, q, \theta]^T$, while the input vector $\boldsymbol{u}_{lon} = [\delta T_1,\ \delta T_2, ...\delta T_n]$ is the throttle command as a percentage of maximum thrust T. The model can be written as:

$$\boldsymbol{M}_{lon}\dot{\boldsymbol{x}}_{lon} + \boldsymbol{G}_{lon}\boldsymbol{x}_{lon} = \boldsymbol{U}_{lon}\boldsymbol{u}_{lon} \tag{2.14}$$

with

$$\boldsymbol{M}_{lon} = \begin{bmatrix} m + \rho\mathcal{V}k_1 & 0 & mr_{CG_3} & 0 \\ 0 & m + \rho\mathcal{V}k_3 & -mr_{CG_1} & 0 \\ mr_{CG_3} & -mr_{CG_1} & J_{CB_y}\left(1 + \rho k'\right) & 0 \\ 0 & 0 & 0 & 1 \end{bmatrix} \tag{2.15}$$

$$\boldsymbol{G}_{lon} = -\begin{bmatrix} X_U & X_W & X_q - mW_0 & (\rho\mathcal{V} - m)g\cos\vartheta_0 \\ Z_U & Z_W & (\rho\mathcal{V} - m)g\sin\vartheta_0 & \\ M_{CB_U} & M_{CB_W} & M_{CB_q} - mU_0 r_{CG_1} - mW_0 r_{CG_3} & mg\left(r_{CG_1}\sin\vartheta_0 - r_{CG_3}\cos\vartheta_0\right) \\ 0 & 0 & 1 & 0 \end{bmatrix} \tag{2.16}$$

$$\boldsymbol{U}_{lon} = \begin{bmatrix} X_{\delta T_i} \\ Z_{\delta T_i} \\ M_{CB_{\delta T_i}} \\ 0 \end{bmatrix} \tag{2.17}$$

$\boldsymbol{U}_{lon}$ matrix, representing the control inputs, will have one column for each motor.

From this representation it is possible to derive the state and control matrices, which leads to the classic formulation of a Linear Time-Invariant (LTI) system:

$$\boldsymbol{A}_{lon} = -\boldsymbol{M}_{lon}^{-1}\boldsymbol{G}_{lon} \qquad \boldsymbol{B}_{lon} = -\boldsymbol{M}_{lon}^{-1}\boldsymbol{B}_{lon} \tag{2.18}$$

$$\dot{\boldsymbol{x}}_{lon} = \boldsymbol{A}_{lon}\boldsymbol{x}_{lon} + \boldsymbol{B}_{lon}\boldsymbol{u}_{lon} \tag{2.19}$$

2.4.2 Lateral-Directional dynamics

The lateral dynamic equation describe the aircraft's motion outside the symmetrical vertical plane. The state variables include lateral velocity, roll and yaw rates, and roll and yaw angle $\boldsymbol{x}_{lat} = [V, p, r, \phi, \psi]^T$. Similar to the longitudinal case, the model can be written as:

$$\boldsymbol{M}_{lat}\dot{\boldsymbol{x}}_{lat} + \boldsymbol{G}_{lat}\boldsymbol{x}_{lat} = \boldsymbol{U}_{lat}\boldsymbol{u}_{lat} \tag{2.20}$$

with

$$\boldsymbol{M}_{lat} = \begin{bmatrix} m + \rho\mathcal{V}k_2 & -mr_{CG_3} & mr_{CG_1} & 0 & 0 \\ -mr_{CG_3} & J_{C\boldsymbol{B}_x} & J_{C\boldsymbol{B}_{xz}} & 0 & 0 \\ mr_{CG_1} & J_{C\boldsymbol{B}_{xz}} & J_{C\boldsymbol{B}_z}\left(1 + \rho k'\right) & 0 & 0 \\ 0 & 0 & 0 & 1 & 0 \\ 0 & 0 & 0 & 0 & 1 \end{bmatrix} \tag{2.21}$$

$$\boldsymbol{G}_{lat} = -\begin{bmatrix} Y_V & Y_p + mW_0 & Y_r - mU_0 & -(\rho\mathcal{V} - m)g\cos(\vartheta_0) & 0 \\ 0 & L_{CB_p} - mW_0 r_{CG_3} & mU_0 r_{CG_3} & -mgr_{CG_3}\cos\vartheta_0 & 0 \\ N_{CB_V} & mW_0 r_{CG_1} & N_{CB_r} - mU_0 r_{CG_1} & mgr_{CG_1}\cos\vartheta_0 & 0 \\ 0 & 1 & \tan\vartheta_0 & \tan\vartheta_0 q_0 & 0 \\ 0 & 0 & 1/\cos\vartheta_0 & q_0/\cos\vartheta_0 & 0 \end{bmatrix} \tag{2.22}$$

$$\boldsymbol{U}_{lon} = \begin{bmatrix} Y_{\delta T_i} \\ L_{CB_{\delta T_i}} \\ N_{CB_{\delta T_i}} \\ 0 \end{bmatrix} \tag{2.23}$$

As in the longitudinal case, $\boldsymbol{U_{lon}}$ matrix, representing the control inputs, will have one column for each motor. We can derive the state and control matrices, as follows.

$$\boldsymbol{A}_{lat} = -\boldsymbol{M}_{lat}^{-1}\boldsymbol{G}_{lat} \qquad \boldsymbol{B}_{lat} = -\boldsymbol{M}_{lat}^{-1}\boldsymbol{B}_{lat} \tag{2.24}$$

$$\dot{\boldsymbol{x}}_{lat} = \boldsymbol{A}_{lat}\boldsymbol{x}_{lat} + \boldsymbol{B}_{lat}\boldsymbol{u}_{lat} \tag{2.25}$$

2.4.3 Augmented Linear Model

The thesis aims to assess various ion engine layouts for control purposes, with these engines positioned around the airship. This setup negates one of the prerequisites for decoupling longitudinal and lateral-directional dynamics: a generalized thrust command can generate forces and moments that impact both longitudinal and lateral dynamics.

The thrust contribution to the linear system in the input matrices $\boldsymbol{B_{lon}}$ and $\boldsymbol{B_{lat}}$ can be derived by performing a first-order Taylor series expansion of Equations (2.10) (2.11) around the trim condition. In the following equations, we account for the contribution of a single engine as example, omitting the subscript (i) for simplicity.

$$\boldsymbol{F}^T \approx \begin{bmatrix} X_0 \\ Y_0 \\ Z_0 \end{bmatrix} + \begin{bmatrix} X_{,\delta T} \\ Y_{,\delta T} \\ Z_{,\delta T} \end{bmatrix} \delta T \tag{2.26}$$

$$\boldsymbol{Q}^T = \boldsymbol{r}_{P_T} \times \boldsymbol{F}^T \tag{2.27}$$

The derivatives computed are:

$$\begin{aligned} X_{\delta T} &= T\cos\sigma\cos\lambda \\ Y_{\delta T} &= T\sin\sigma \\ Z_{\delta T} &= T\cos\sigma\sin\lambda \\ L_{CB_{\delta T}} &= y_{P_T}Z_{\delta T} - z_{P_T}Y_{\delta T} \\ M_{CB_{\delta T}} &= z_{P_T}X_{\delta T} - x_{P_T}Z_{\delta T} \\ N_{CB_{\delta T}} &= x_{P_T}Y_{\delta T} - y_{P_T}X_{\delta T} \end{aligned} \tag{2.28}$$

Due to this reason, the decoupled models presented in previous sections are restructured into a unified 9-equation model that incorporates both dynamics, interconnected by the thrust terms found in the input matrix. The updated state vector is represented as $\boldsymbol{x_{tot}} = [U, W, q, \theta, V, p, r, \phi, \psi]^T$ while the input vector remains the same $\boldsymbol{u}_{lon} = [\delta T_1, \delta T_2, ...\delta T_n]^T$. The mass, state and input matrices for the revised system are defined as follows:

$$\boldsymbol{M}_{tot} = \begin{bmatrix} \boldsymbol{M}_{lon} & \mathbf{0} \\ \mathbf{0} & \boldsymbol{M}_{lat} \end{bmatrix} \qquad \boldsymbol{A}_{tot} = \begin{bmatrix} \boldsymbol{A}_{lon} & \mathbf{0} \\ \mathbf{0} & \boldsymbol{A}_{lat} \end{bmatrix} \qquad \boldsymbol{B}_{tot} = \begin{bmatrix} \boldsymbol{B}_{lon} \\ \boldsymbol{B}_{lat} \end{bmatrix} \tag{2.29}$$

3. Thrusters Layout

The choice of propulsion greatly affects airship size and design. Traditionally, LTAs used diesel engines, typically ranging from 150 to 500 horsepower. These types of engines are complex, heavy and do not allow very responsive control. In recent times, airships equipped with traditional electric motors have been proposed. These motors offer enhanced maneuverability due to their readily available torque and easy control.

This thesis focuses on the integration of ion engines (EHD thrusters). These engines, thanks to the absence of moving parts, can be a breakthrough in reliable control of airships. They will be strategically placed in belts around the aircraft, primarily for dynamic control functions. To overcome current power limitations, a traditional electric motor will be located at the rear of the airship. The electric motor, positioned centrally with respect to the $(b2,b3)_{\mathcal{B}}$ axes and at the tail of the aircraft, will have the main thrust function, while the ion engines will ensure control.

3.1. Ion thrusters

EHD thrusters, harness the Corona effect, a gas discharge phenomenon. This effect concentrates ionization in a high-field ionization region near an active electrode due to its geometry. Thanks to the Corona discharge, in a region called the drift area, electrons and ions interact with neutral air without acquiring enough energy to ionize. This region lies between two electrodes and is outside the ionization zone.

The core of an EHD propulsion system is its two electrodes, the emitter and collector, separated by a gap and linked to a high-voltage source. The emitter's sharp curvature generates ions in a cold plasma due to its strong electric field. The collector, with a larger surface area, experiences significant aerodynamic drag caused by the surrounding ionic wind.[1]

Typically, EHD thrusters adopt a triangular shape. They are composed of a tautly held conductive wire above a vertical aluminum foil, oriented with one of its thin edges facing the wire. These components are secured within a lightweight non-conductive frame. An ionic wind is generated by maintaining a sufficiently high voltage between the wire and foil. [1, 2, 19]

In laboratory peak thrust-to-power ratios of greater than 100 N/kW have been observed [10], whereas the value for a typical jet aircraft engine is in the order of 2 N/kW.

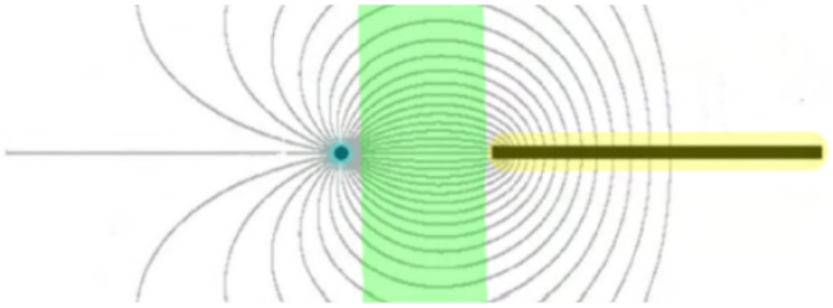

Figure 3.1: Scheme of a EHD thruster. In light-blue the ion source, a wire with corona effect, in green the drifting zone and in yellow the collector [19]

3.2. Model of thrusters

In this thesis, all the engines are treated as black boxes generating thrust. Their operation is modeled through first-order dynamics. Consequently, the governing transfer functions $\boldsymbol{T_{ion}}(s)$ and $\boldsymbol{T_{main}}(s)$ for their operation are as follows:

$$\boldsymbol{T_{ion}}(s) = \delta T_{ion} T_{ion} \left[\frac{1}{1 + \tau_{ion} s} \right] \tag{3.1}$$

$$\boldsymbol{T_{main}}(s) = \delta T_{main} T_{main} \left[\frac{1}{1 + \tau_{main} s} \right] \tag{3.2}$$

Where δT_{ion} and δT_{main} are the throttle command as a percentage of maximum thrust T_{ion} and T_{main}. While τ_{ion} and τ_{main} denote the respective time constants associated with the engines. The maximum power outputs and time constants used in this thesis for each thruster will be:

$$\begin{aligned} T_{ion} &= 400 \text{ [N]} \\ T_{main} &= 300 \text{ [N]} \\ \tau_{main} &= 0.1 \text{ [s]} \\ \tau_{main} &= 1 \text{ [s]} \end{aligned} \tag{3.3}$$

From the time the controller gives the command to start an engine the thrust will stabilize at the target value in approximately 3 seconds for the main propeller and 0.3 seconds for the ion engines.

3.2.1 State Space model

A simple state space representation of the engine dynamics is:

$$\dot{\boldsymbol{x}}_{eng} = \boldsymbol{A}_{eng} \boldsymbol{x}_{eng} + \boldsymbol{B}_{eng} \boldsymbol{u}_{eng} \tag{3.4}$$

where A_{eng} and B_{eng} are diagonal matrices composed with the time constants of the motors as follow:

$$\boldsymbol{A_{eng}} = -diag\,(\frac{1}{\tau_1}, \frac{1}{\tau_2}, ... \frac{1}{\tau_n}); \qquad \boldsymbol{B_{eng}} = diag\,(\frac{1}{\tau_1}, \frac{1}{\tau_2}, ... \frac{1}{\tau_n}); \tag{3.5}$$

The model described in equation (2.29) is augmented to include motor dynamics:

$$\begin{bmatrix} \dot{\boldsymbol{x}}_{eng} \\ \dot{\boldsymbol{x}}_{tot} \end{bmatrix} = \begin{bmatrix} \boldsymbol{A}_{eng} & \boldsymbol{0} \\ \boldsymbol{B}_{tot} & \boldsymbol{A}_{tot} \end{bmatrix} \begin{bmatrix} \boldsymbol{x}_{eng} \\ \boldsymbol{x}_{tot} \end{bmatrix} + \begin{bmatrix} \boldsymbol{B}_{eng} \\ \boldsymbol{0} \end{bmatrix} \boldsymbol{u}_{eng} \tag{3.6}$$

In the new model (3.6), $\boldsymbol{u}_{eng}$ represents the instantaneous actuator comand. As it traverses the motor dynamics, generates the signal $\boldsymbol{x}_{eng}$, that act as control signal of the original system.

3.3. Three types of layouts

All configurations are equipped with a central rear electric motor, positioned at the same location as the original Lotte airship engine, the aircraft selected as a baseline (more detail in section 4.1). The ion engines are arranged in belts encircling the airship's envelope. To maintain contact between the anode and cathode and the airship's surfaces, these ion engines are tangentially aligned with the airship's contour. The angles of the motors relative to $b_{1\mathcal{B}}$ axis can be observed in Figure 3.3.

In our experimentation, we considered three distinct engine arrangement, as illustrated in the Figure 3.2.

- Layout 1 is equipped with a single belt of 4 ion thrusters, positioned at 90° from each other (Figure 3.2a);
- Layout 2 features a single belt with 8 ion thrusters, positioned at 45° from each other (Figure 3.2b);
- Layout 3 is equipped with 8 ion thrusters positioned on two different belts like those of layout 1, one positioned at the bow and one at the stern of the airship (Figure 3.2c).

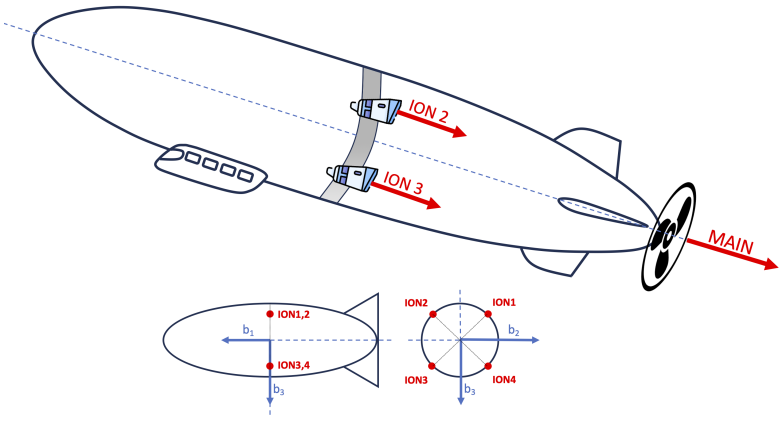

(a) Layout 1

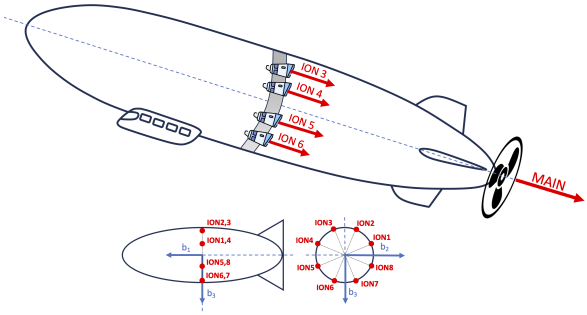

(b) Layout 2

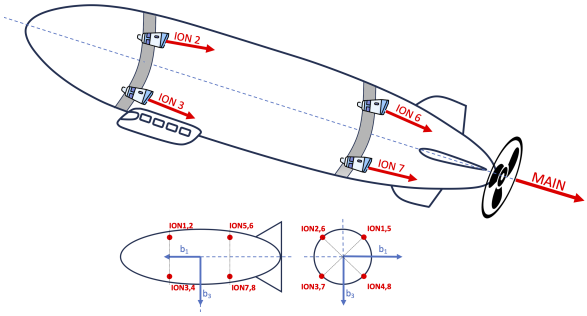

(c) Layout 3

Figure 3.2: thrusters configurations

The objective of these three configurations is to investigate whether increasing the granularity of thrust point discretization can lead to a substantial enhancement in maneuverability. These belts are subsequently positioned at various locations on the airship to assess how maneuverability is affected by the position of the ion thrusters.

3.3.1 Belt displacement along the airship

The Lotte airship measures 16 meters in length (15m the envelope). Starting from the center of buoyancy CB, a total of nine distinct planes were delineated for the belt placements. Four plane toward the aft section ($b_{1\mathcal{B}}$=-6m, $b_{1\mathcal{B}}$=-4.5m, $b_{1\mathcal{B}}$=-3m, and $b_{1\mathcal{B}}$=-1.5m), four positions towards the bow ($b_{1\mathcal{B}}$=1.5m, $b_{1\mathcal{B}}$=3m, $b_{1\mathcal{B}}$=4.5m, and $b_{1\mathcal{B}}$=6m), and the central plane ($b_{1\mathcal{B}}$=0m). The planes are numbered in red in figure 3.3, where the angles of the envelope with respect to the $b_{1\mathcal{B}}$ axis and their distance from CB are also indicated.

In configurations 1 and 2 the single belt was evaluated in all nine positions. In the third configuration the belts were initially positioned at the ends and then progressively moved in the opposite direction (First experiment with belts at positions 1 and 9, the second experiment with belts at positions 2 and 8, and so forth).

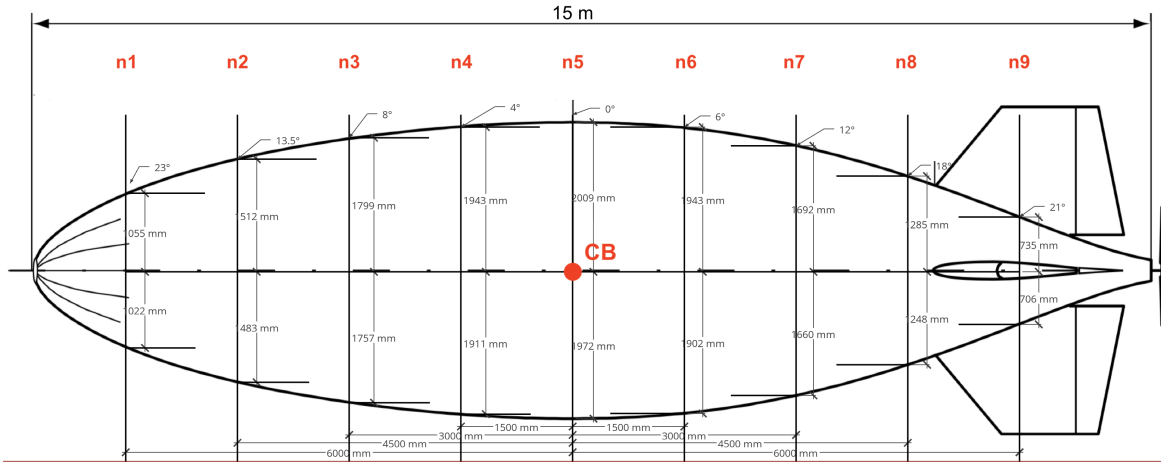

Figure 3.3: Belt displacement along the Lotte airship

For clarity and conciseness in identifying each of the 27 possible configurations, the following notation will be used: "layout$\boldsymbol{x}$-n$\boldsymbol{y}$". Here, "x" denotes one of the three possible belt arrangements (1, 2, 3), and "n" represents their position (1, 2, 3, 4, 5, 6, 7, 8, 9).

4. Linear model validation

The validation of the MATLAB-implemented linear model involves a comparison between system eigenvalues and existing literature data. For conventional airships, eigenvalue maps typically exhibit regular patterns.

4.1. Lotte airship

The simulations utilize the Lotte airship's geometry and aerodynamic coefficients as input data. This aircraft, a non-rigid, solar-powered LTA, has been extensively studied and tested at the University of Stuttgart's Institute of Flight Mechanics and Control during the 1990s and early 2000s [6, 7]. Its abundant, reliable data, rarely found in LTA literature, facilitates realistic computations. The nonlinear model described in Section 2 is simulated in matlab incorporating Lotte's geometry coefficients.

A significant change from the Lotte design is the thrusters configuration. While the original prototype utilizes a single propeller in the tail, this revised configuration retains a similar propeller as the main engine but incorporates additional ion thruster belts as described in Section 3.3. In the tail section the mobile control surfaces have been maintained for stabilization, without any moving parts.

From an inertia standpoint, these changes influences mass, static and moment of inertia values, as well as different positioning of the CG. In this thesis, we simplify by treating them as constant regardless of design variations.

Basic specifications of the Lotte airship are described in Table 1:

Parameter	Value
Volume $\mathcal{V}$ [m^3]	107.42
Lenght [m]	16.0
Max. diameter [m]	4.0
Tail span [m]	4.6
Mass m [kg]	136.8
Max Airspeed [m/s]	12

Table 1: Basic specifications of Lotte airship [7].

4.2. Equilibrium and trim solution

Reference conditions for horizontal forward flight were established starting from the original airship's range. These conditions are set at 6 m/s airspeed and an altitude of 200 meters.

For each configuration a model has been derived solving equation (2.13). This trimming process involves solving Equation (1) under steady-state conditions ($\dot{\boldsymbol{V}}, \dot{\boldsymbol{\omega}} = 0$) during symmetric, horizontal, forward flight. The trim solution provides values for the body components of airspeed (U_0 and W_0), as well as a pitch angle (θ_0), with all other state array components forcefully set to zero.

Equilibrium values $\boldsymbol{\delta T_i}$ are found as part of the trim problem solution. Since there are many engines available, the trim problem admits multiple solutions. The solver employed (lsqnonlin in MATLAB) was configured to favor the main propeller for achieving equilibrium, in order to prioritize the use of ion thrusters for dynamic control. The approach was effective and in all the trimmed models the equilibrium control for ion engines never never exceeds 3%.

From these equilibrium values linearized models (2.19) and (2.25) are calculated. Note that since all the terms concerning the engines are present in the B matrices, the A matrices representing the dynamics of the airship are independent from the configuration used. The eigenvalue analysis carried out in the next section is therefore valid for all tested configurations.

4.3. Longitudinal and Lateral modes for a traditional airship

Pole plot for typical large nonrigid airship [5, 11] is shown in figure 4.1:

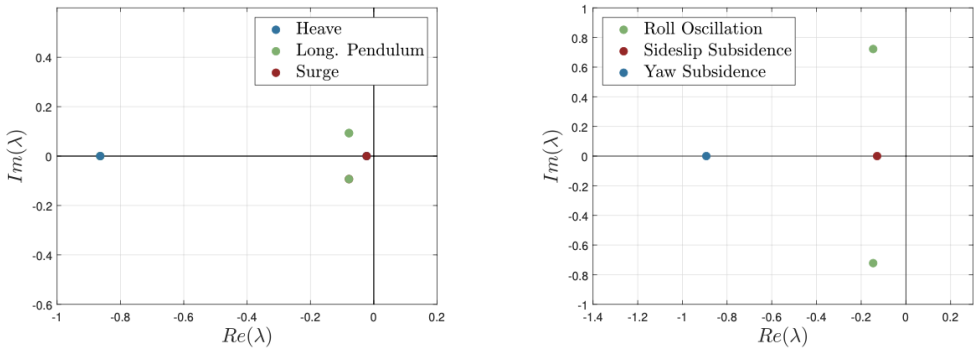

(a) Longitudinal dynamics.

(b) Lateral dynamics.

Figure 4.1: Root Locus for a conventional large airship.

The longitudinal dynamics are characterized by three distinct modes:

- **Surge Mode**: This mode is represented by a real pole with a very long time constant that decrease with speed. It describe a stable, non-oscillatory motion. It is linked to perturbations in longitudinal velocity (U).
- **Heave/Pitch Subsidence Mode**: This mode, represented by a real pole with a shorter time constant, describe a motion damping in vertical velocity (W). As speed increase it also interact with perturbation in pitch rate (q).
- **Longitudinal Pendulum Mode**: Characterized by a pair of complex roots, this mode represent a low-frequency motion with low damping. It resembles the periodic motion of the center of gravity swinging below the center of buoyancy. It couples with heave motion at higher speeds, influenced by fins and hull aerodynamics. This mode is particularly sensitive to perturbations in vertical velocity (W) and pitch rate (q).

Also the lateral dynamics are characterized by three distinct modes:

- **Yaw Subsidence Mode**: It is represented by a real eigenvalue that decrease it's time constant with speed. It couples with the Sideslip Subsidence Mode through perturbations in lateral velocity (V) and yaw rate (r).
- **Sideslip Subsidence Mode**: it corresponds to another real eigenvalue with longer time constant. It exhibits stable exponential settling of lateral velocity (V). As speed and aerodynamic effects increases, it reduce the settling time.
- **Roll Oscillation Mode**: Characterized by a pair of complex roots with low damping, it represent oscillation around the $b_{1\mathcal{B}}$ axis, linked to roll rate (p). Buoyancy and gravity impact it, and damping improves with speed as fins contribute more to roll damping.

4.4. Lotte eigenvalues analysis

The code results are compared to a sensitivity analysis based on Lotte airship data from the literature (Figure 4.2c-4.2d). This analysis involved computing eigenvalues while varying the longitudinal trim velocity (U_0) from 2m/s to 12m/s. The system, as trimmed in this thesis at 6m/s, displays a pole map of the linearized model as it is expected (Figure 4.2a-4.2b).

However, an unconventional behavior is observed in the Longitudinal Pendulum and Lateral Sideslip Subsidence modes when compared to typical airships. This behavior is typical of Lotte itself [6].

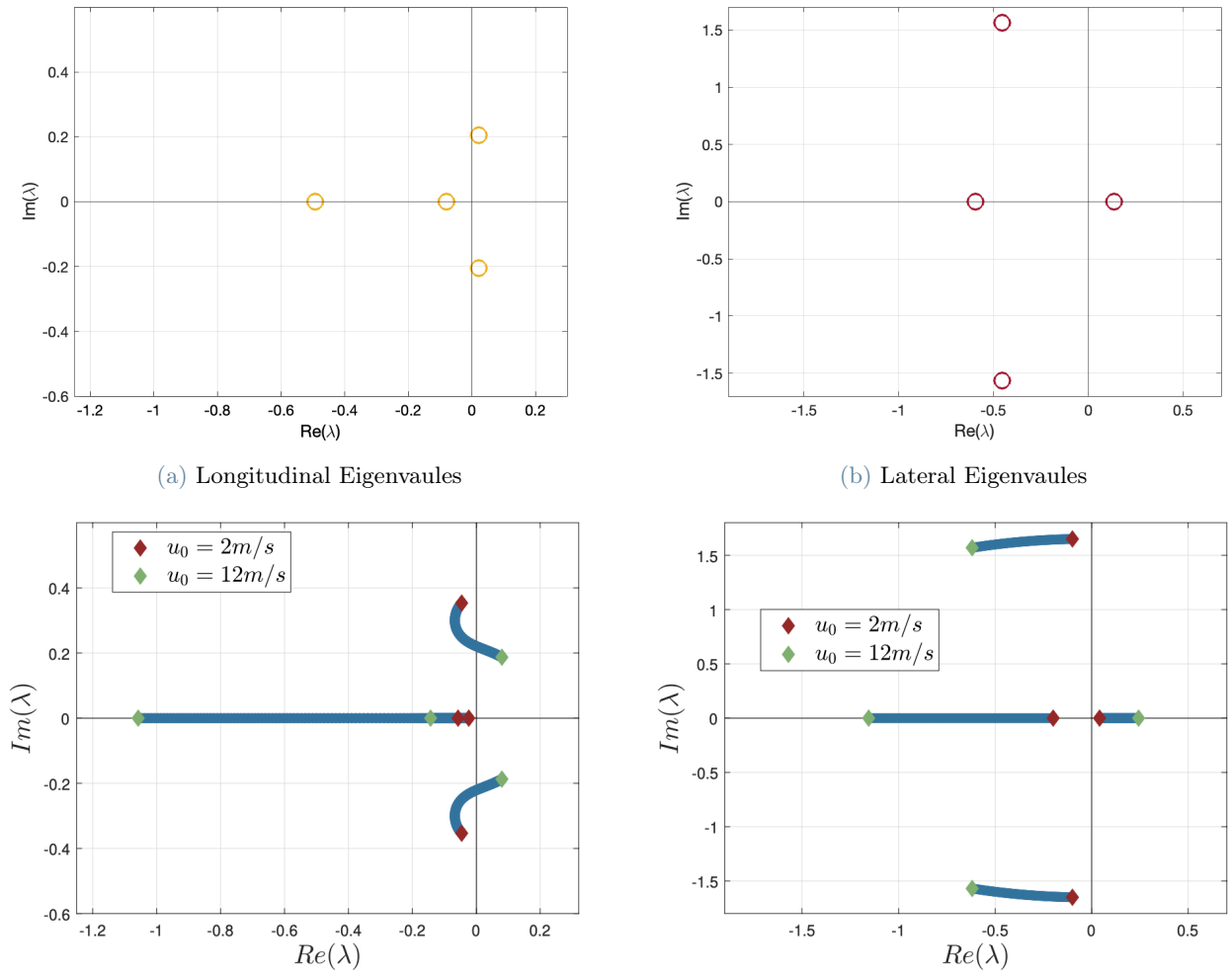

(a) Longitudinal Eigenvaules

(b) Lateral Eigenvaules

(c) Longitudinal sensitivity analysys

(d) Lateral sensitivity analysys

Figure 4.2: Lotte eigenvalues

4.5. Step responses

The following simulation results pertain to a a linear model of the Lotte airship, with an arrangement of engines Layout1-n5. In this configuration there is only one belt equipped with 4 ion thrusters, positioned at 90° from each other, arranged centrally to the airship, as well as a rear main propeller. The described configuration is represented in Figure 3.2a.

To validate the proper operation of the ion thrusters for executing pitch and yaw rotations (around the $b_{2\mathcal{B}}$ and $b_{3\mathcal{B}}$ axes) and to assess potential interference with other states, two experiments were set up.

The analysis lasts 5 seconds and involve only Steady-State Flight conditions with small perturbations around a trim state ($\delta(\phi,\theta,\psi)$<10°; $\delta(p,q,r)$<3°/s; $\delta(U,V,W)$<0.1 m/s). This ensures that the observations fall within the linear model's validity range. In LTA aircrafts the non-linearities of the model become relevant during maneuvers, such as turns, variations in angle of attack, and leeway [3].

4.5.1 Yaw Rotation

In this experimental setup, a step input δT_i of 0.25 is applied to the engines located on the port side (ION2 and ION3), while an equivalent step input of -0.25 is administered to the starboard side engines (ION1 and ION4). The main engine is maintained at its equilibrium position.

After five seconds into the experiment, the airship's yaw rate (r) reached 3°/s, resulting in a 10° turn of the aircraft. As evident from the time series in Figure 4.3, the rotation around the yaw axis did not excite the longitudinal dynamics. The only states that exhibited alterations are $\boldsymbol{x}_{lat} = [V, p, r, \phi, \psi]^T$.

It can be also seen the diverging behaviour of Yaw Subsidence Mode which, triggered by the yaw rate excitation (r), led to a lateral velocity variation (V). Additionally, it is evident the Roll Oscillation Mode causing the airship to oscillate around the $b_{1\mathcal{B}}$ axis. (Figure 4.3c 4.3b)

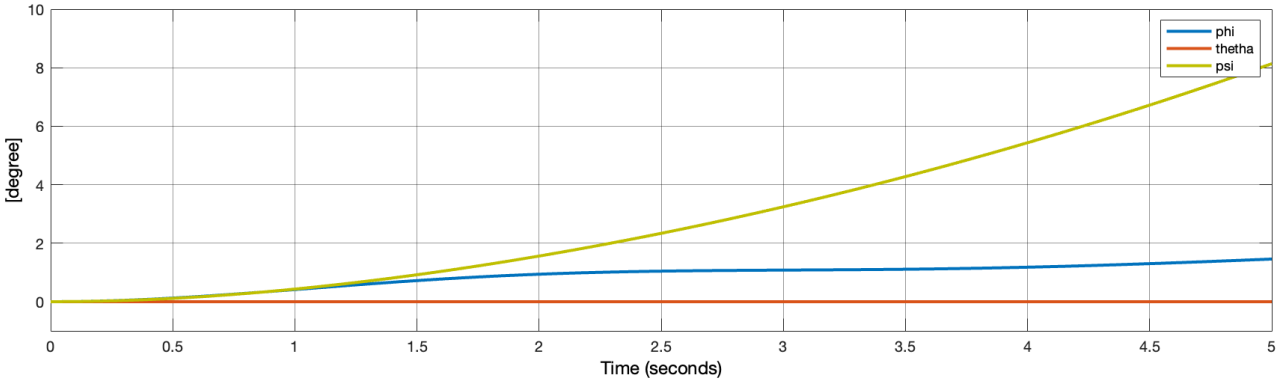

(a) Angles

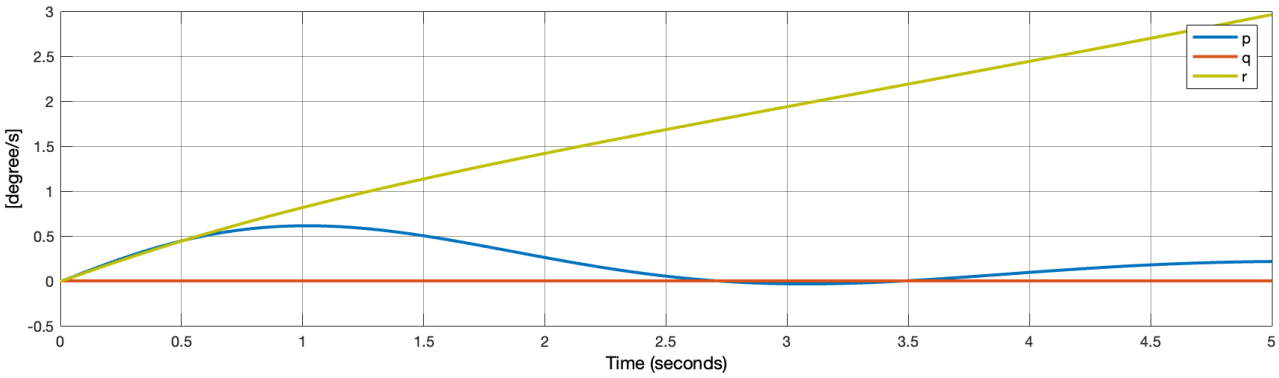

(b) Angular velocities

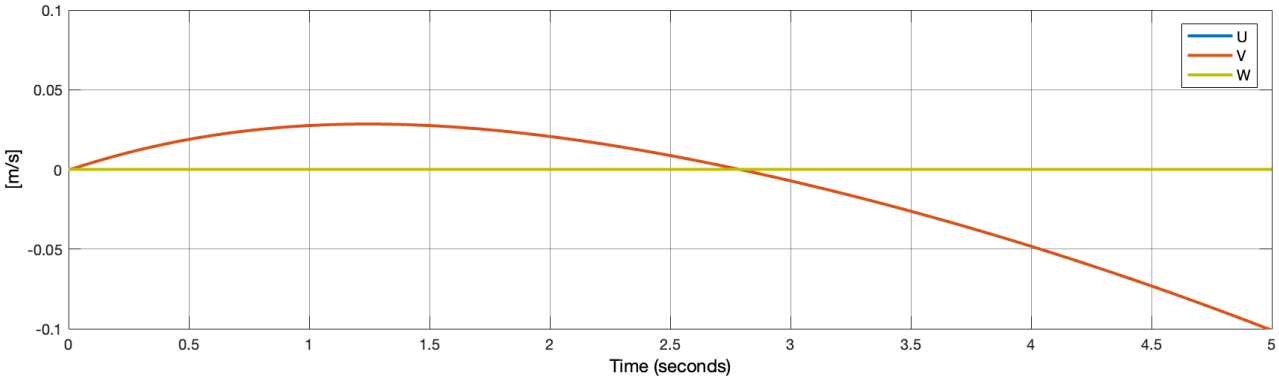

(c) Linear velocities

Figure 4.3: Yaw rotation

4.5.2 Pitch Rotation

Similar to the previous experiment, δT_i 0.25 steps are applied to the four ion thrusters, positively to the two lower engines (ION3 and ION4) and negatively to the two upper engines (ION1 and ION2). The main engine is maintained at its equilibrium position.

After five seconds into the experiment, the airship's pitch rate (q) reached $2°/s$, resulting in a $7°$ turn of the aircraft. Also in this experiment the model remained decoupled: when the pitch angle is excited the lateral dynamics remained unaffected (Figure 4.4). The only states that exhibited alterations are $\boldsymbol{x}_{lon} = [U, W, q, \theta]^T$.

It is worth noting the impact of the Longitudinal Pendulum Mode, as the introduction of a pitch rate variation causes diverging perturbations in both the U and V velocities (Figure 4.4c).

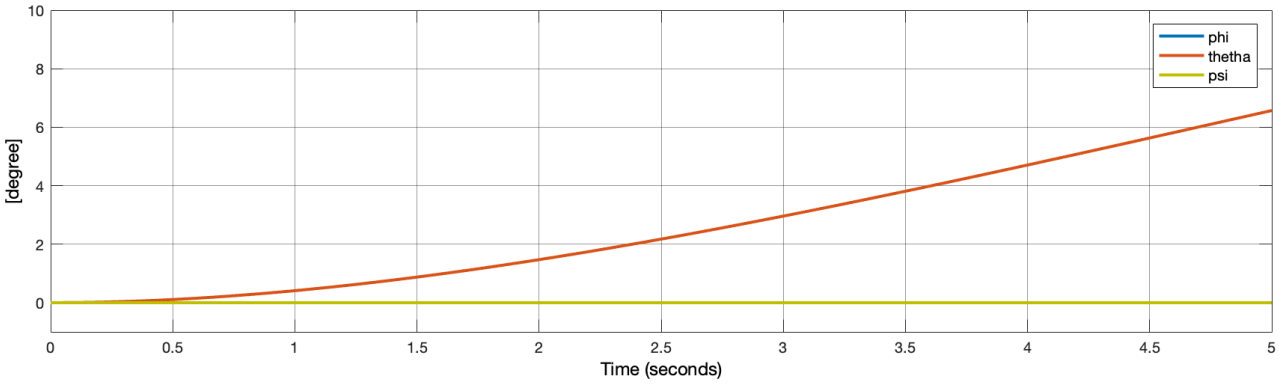

(a) Angles

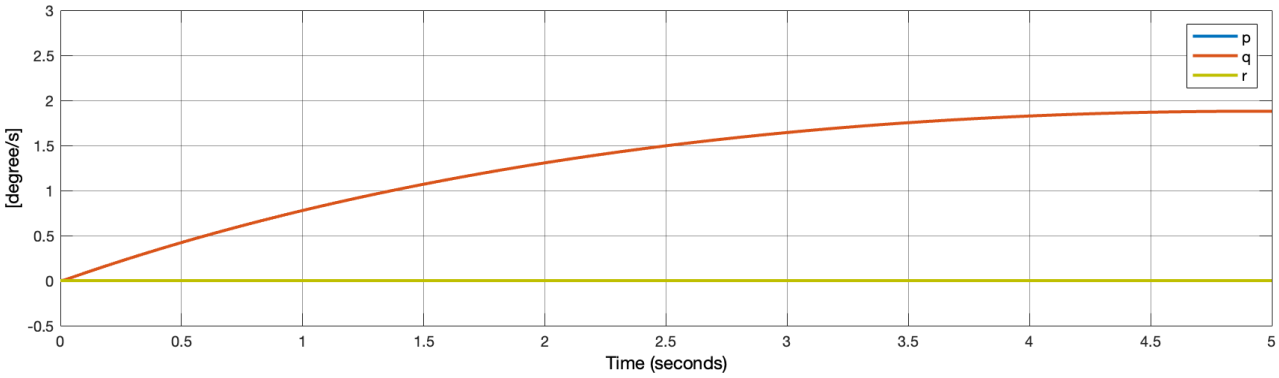

(b) Angular velocities

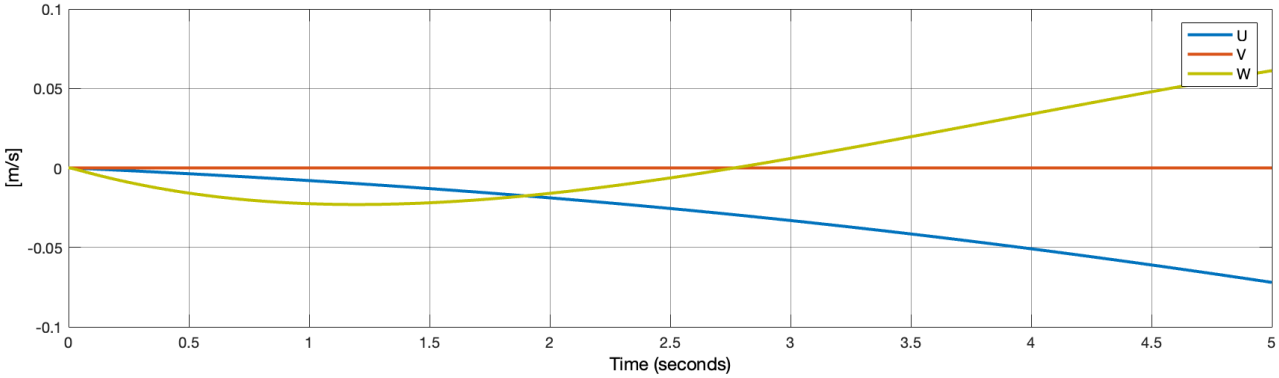

(c) Linear velocities

Figure 4.4: Pitch rotation

5. Control

5.1. Linear Quadratic Regulator

The Linear Quadratic Regulator (LQR) is a widely recognized method for determining optimal feedback control gains [9, 12]. It operates on the principle of optimizing the control by minimizing the quadratic cost function (5.1), finding a control input that minimizes the weighted sum of the system's state variables and control effort over an infinite time horizon. It is a state feedback regulator, its general operating scheme is:

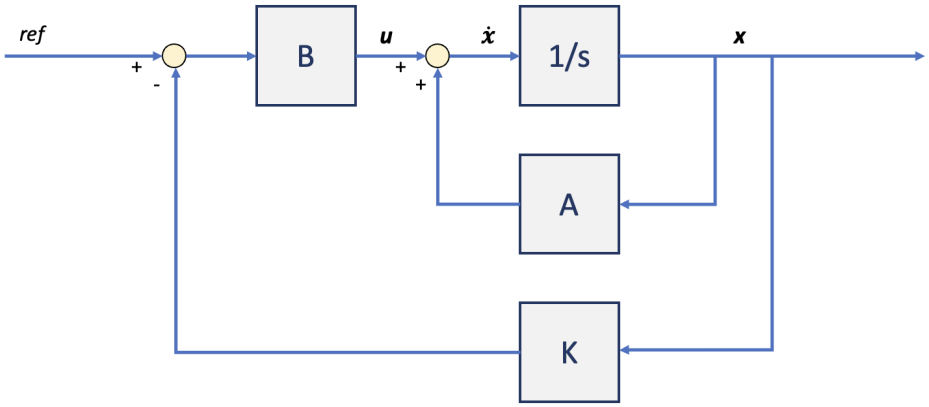

Figure 5.1: General Scheme For Linear Quadratic Regulator

$$\boldsymbol{J}\left(x_t, u_t\right) = \int_0^{\infty} \left(x(t)^T \boldsymbol{Q} x(t) + u(t)^T \boldsymbol{R} u(t)\right) dt \tag{5.1}$$

In the cost function (5.1), $Q \geq 0$ and $R > 0$, respectively positive-semidefinite and positive-definite matrices, weight the importance of different states and inputs. The careful selection of these matrices is crucial in meeting transient response requirements and imposing constraints on state variable magnitudes and control effort.

Matrix Q assigns significance to each state variable concerning others. When the magnitude of Q is increased, the regulator places more emphasis on minimizing the tracking error, resulting in a smaller error in the system's response. However, this increased emphasis on precision demands a higher control force $u(t)$. Matrix R symbolizes the cost linked to each control actuator. When the values in R are augmented, it promotes the reduction of the corresponding control input, at the expense of other inputs and the overall dynamic response of the system.

After selecting the appropriate Q and R matrices, LQR gains were computed with MATLAB function $K = lqr(A, B, Q, R)$. The state feedback control signal to stabilize the system is:

$$\boldsymbol{u}(t) = \boldsymbol{K}\boldsymbol{x}(t) \tag{5.2}$$

5.2. Defining Q and R

To facilitate the tuning of the regulator matrices Q and R, a decision was made to employ diagonal matrices, chosen for their simplicity and ease of adjustment. In this configuration, each element on the diagonal of Q corresponds to the weighting for an individual state, while each element on the diagonal of R represents the cost associated with utilizing a specific actuator.

The controller specifications were established with the objective of providing responses to both longitudinal and lateral perturbations, aiming to achieve equitable noise rejection in all directions. Lateral speed W and yaw

rate r had to be weighted more than others. Instead, given the main thruster, the U state was underweighted, respect W and V. It was also observed that a better control of rotational dynamics is achieved by assigning significant weights to the rates (p, q, r) and relatively lesser weights to the angles themselves (θ, ϕ, ψ).

To minimize control saturation during experimental tests, the control strategy was designed to avoid excessive demands on the motors. In the experimental setup, shown in Figure 5.2, a saturation limit was implemented, preventing the engines from providing power beyond maximum levels. During aggressive maneuvers, such as those in Experiment 7 (6.1), the control system temporarily saturates the actuators while still achieving effective stabilization.

The central main propeller, despite its location along the $b_{1\mathcal{B}}$ axis, can exert influence on the pitch rate q and consequently affect longitudinal dynamics. The primary objective was to prioritize ion thrusters for directional control, while relying on the main propeller for longitudinal velocity control. It was observed that the control strategy automatically favored the use of ion engines arranged in a belt formation to enhance disturbance rejection, even if less powerful. Consequently, in the Q matrix, the main engine was weighted more than the ion engines.

After tuning the design parameters through a process of trial and error, the state weights implemented in the Q matrix are:

$$\begin{array}{lll} Q_U = 100 & Q_W = 800 & Q_V = 500 \\ Q_q = 100 & Q_p = 100 & Q_r = 1000 \\ Q_\theta = 10 & Q_\phi = 10 & Q_\psi = 10 \end{array} \tag{5.3}$$

In the augmented system outlined in equation (3.6), each engine's dynamics has a dedicated state. To ensure flexibility and not constrain the control possibilities, all Q_i that weight these states were deliberately set to zero.

The weight of matrix R, associated with ion engine input and main engine input are:

$$R_{ion} = 40, \qquad R_{main} = 40 \tag{5.4}$$

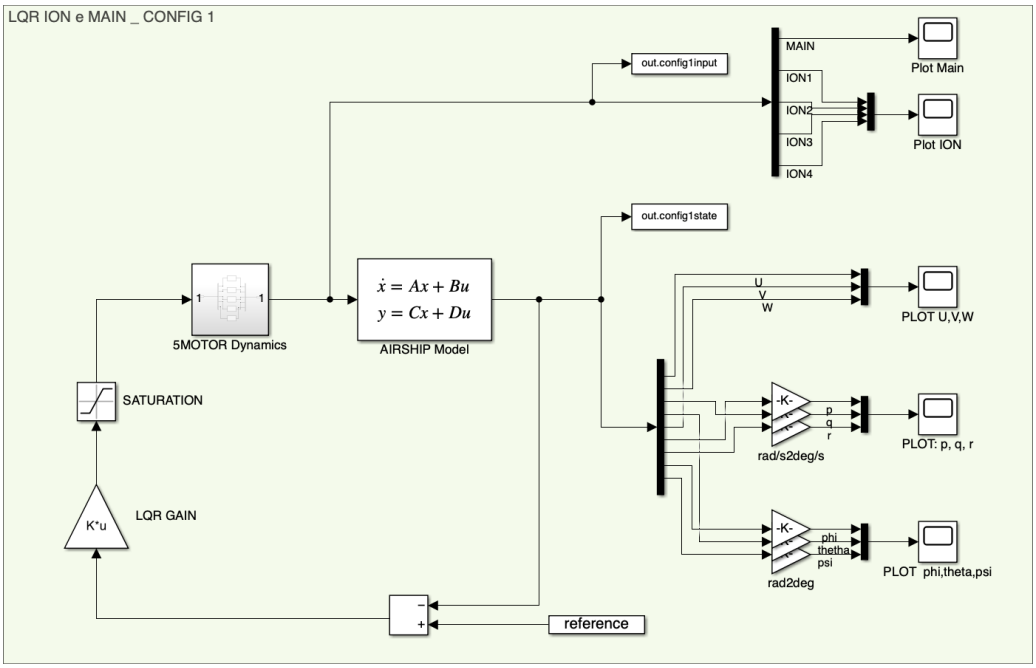

Figure 5.2: Simulink Experimental setup for Layout 1

For each of the 27 possible configurations (explained in section 3.3.1), a specific LQR controller will be computed. All the different regulator will aim to minimize the common cost function.

5.3. Simulations

To illustrate the effective decoupling of variables, successful control outcomes, and the operation of the controllers across various configurations, we present a single experiment conducted in several pivotal configuration. Starting from stable, horizontal, and trimmed flight, this experiment excites angular rates p, q, and r at $3°/s$. The control system swiftly restores the initial equilibrium.

As an illustrative example, for layout 1, we present the results achieved by the controllers with the belt positioned at n2, n5, and n8 (Figure 5.3). Likewise for layout 2 (Figure 5.4). In the case of layout 3, which exhibits symmetry, we showcase the results for the belts positioned at n7 and n9 (Figure 5.5).

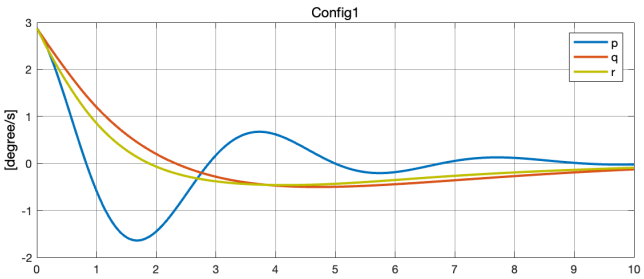

(a) Layout1-n2 p, q, r

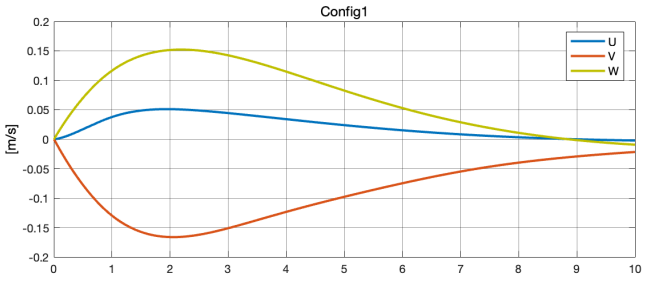

(b) Layout1-n2 U, V, W

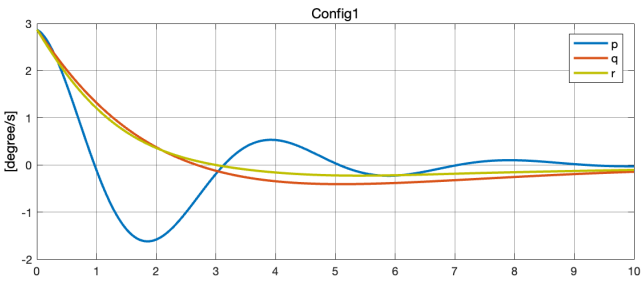

(c) Layout1-n5 p, q, r

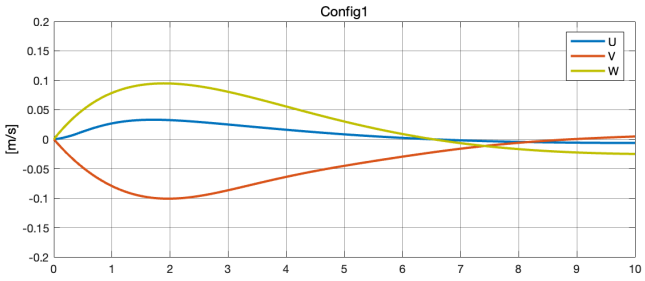

(d) Layout1-n5 U, V, W

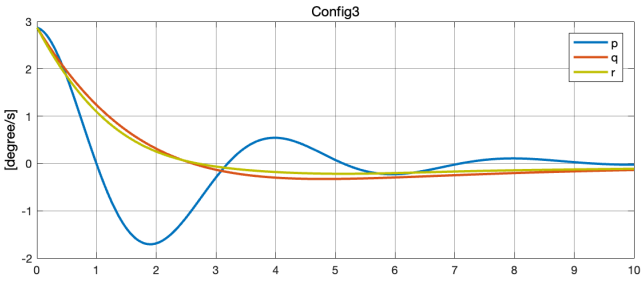

(e) Layout1-n8 p, q, r

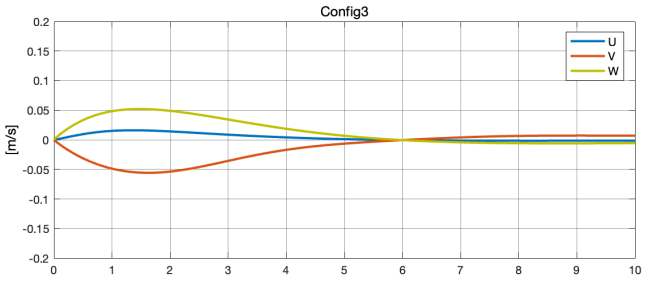

(f) Layout1-n8 U, V, W

Figure 5.3: 4 Ion motors in one belt. Positioned at the bow, in the center and at the stern.

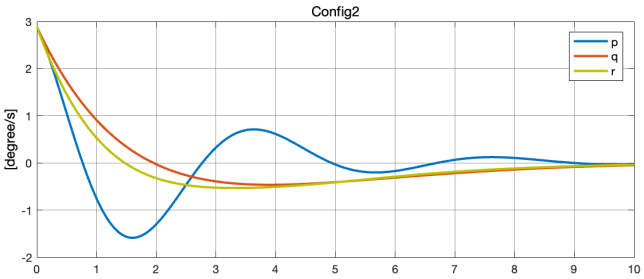

(a) Layout2-n2 p, q, r

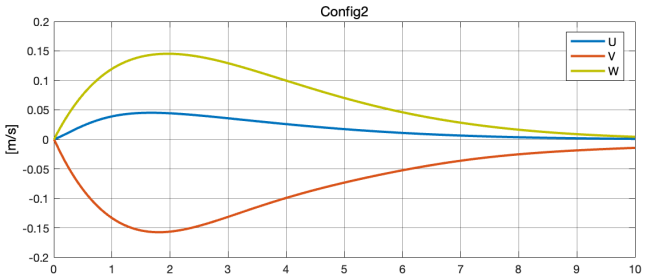

(b) Layout2-n2 U, V, W

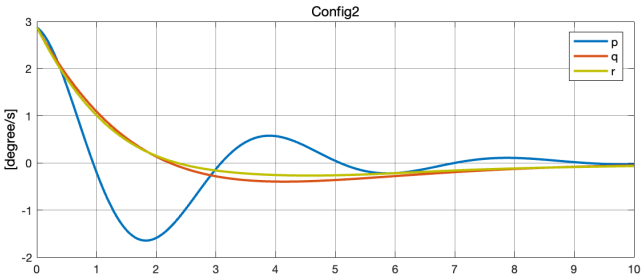

(c) Layout2-n5 p, q, r

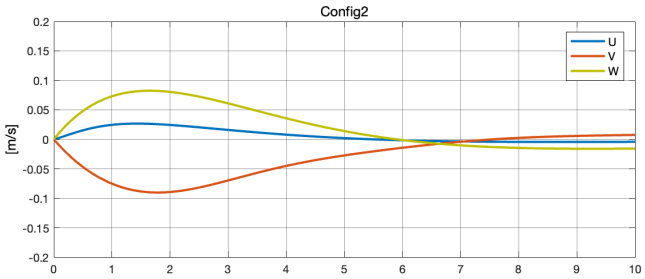

(d) Layout2-n5 U, V, W

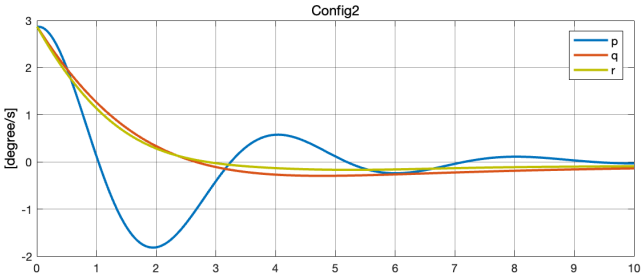

(e) Layout2-n8 p, q, r

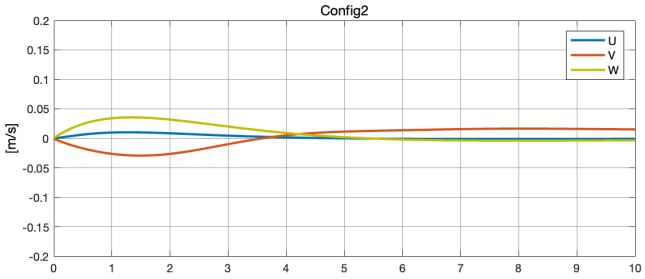

(f) Layout2-n8 U, V, W

Figure 5.4: 8 Ion motors in one belt. Positioned at the bow, in the center and at the stern.

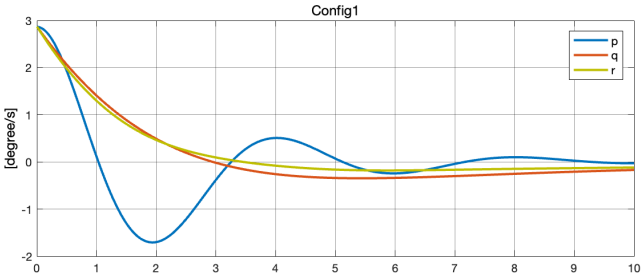

(a) Layout3-n7 p, q, r

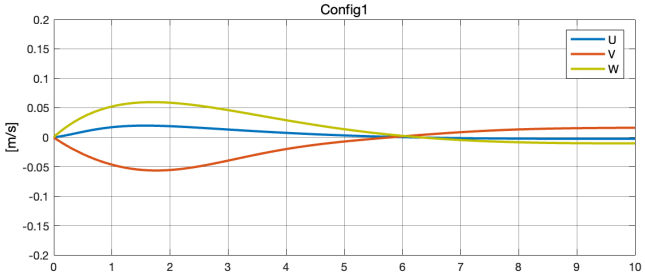

(b) Layout3-n7 U, V, W

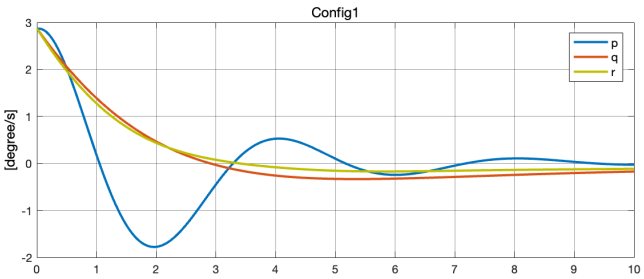

(c) Layout3-n9 p, q, r

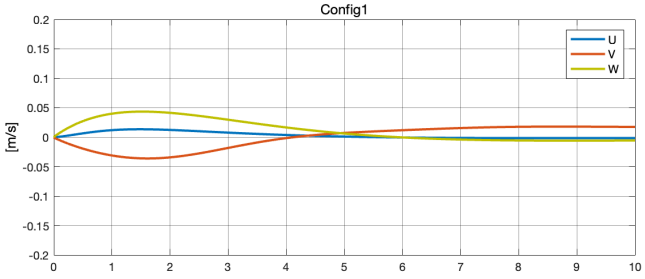

(d) Layout3-n9 U, V, W

Figure 5.5: 8 Ion motors divided into two belts positioned at different distances

6. Layout comparison

The central objective of this thesis is to find an optimal methodology for designing thrust-based control airships. In order to gain a comprehensive understanding of the strengths and weaknesses inherent in different thruster configurations, it is essential to select a set of experiments that will be replicated across all configurations. Additionally, the establishment of a quantifiable benchmark is crucial to evaluate the performance of each specific thruster configuration.

In the starting scenario the airship is in stable, horizontal, and trimmed flight. In the event of external disturbances, the system, operating in a closed-loop configuration, will initially deviate its state and control signals from their predefined reference values. These deviations are subsequently mitigated, ultimately restoring the system to its initial equilibrium. The effectiveness of this process hinges both on the responsiveness of the control dynamics and on the power of the control input to influence the state.

6.1. Selected Experimental Trials

It was determined to execute seven distinct experiments on each configuration, in order to analyse the response on every different dynamic. The first six experiments consist of perturbing the states relating to linear and angular speeds ($\boldsymbol{V}$,$\boldsymbol{\omega}$) one at a time and let closed-loop control bring them back to equilibrium. The seventh experiment involves simultaneously perturbing all the states.

The experiments start with a straight, horizontal, steady flight of 6m/s and is perturbed as follow:

$$\begin{aligned} \Delta U &= 0.5\,[\mathrm{m/s}] \\ \Delta V &= 0.5\,[\mathrm{m/s}] \\ \Delta W &= 0.5\,[\mathrm{m/s}] \\ \Delta p &= 3\,[^\circ/\mathrm{s}] \\ \Delta q &= 3\,[^\circ/\mathrm{s}] \\ \Delta r &= 3\,[^\circ/\mathrm{s}] \end{aligned} \tag{6.1}$$

$$\Delta U = \Delta V = \Delta W = 0.5\,[\mathrm{m/s}], \quad \Delta p = \Delta q = \Delta r = 3\,[^\circ/\mathrm{s}]$$

Each experiment has a duration of 10 seconds, with a fixed time step of 0.01 seconds for each computational iteration.

6.2. Benchmark used for comparison

To ensure a meaningful comparative analysis among different thruster configurations, a uniform approach is employed. The Linear Quadratic Regulator (LQR) is employed as control strategy, with the overarching goal of

minimizing a cost function that consider control costs and dynamic performance. The same weights have been used across all configurations so all the regulators will try to minimize the same function. Configurations that offer enhanced maneuverability will enable the controller to achieve more efficient solutions than configurations that allow for less maneuverability. Thus, the decision is made to employ the cost function as the benchmark for assessing configuration quality, as already done in literature [16, 17].

The benchmark, normalized for the duration of the experiment, is defined as follows:

$$\boldsymbol{J_{exp}} = \frac{1}{N} \sum_{\tau=0}^{N-1} \left(x_\tau^T \boldsymbol{Q} x_\tau + u_\tau^T \boldsymbol{R} u_\tau \right) \tag{6.2}$$

where Q and R are the weight matrices of the LQR controller, $\mathbf{x}_\tau$ and $\mathbf{u}_\tau$ are respectively the state vector and the input vector for each step τ, N is the number of simulation steps.

6.3. Analysis of the results

The outcomes of the 189 conducted experiments are presented in graphical way in Figure 6.2. These experiments have been categorized based on their respective type. Each graph show the experiment benchmark results for all tested configurations.

From the obtained results, we can derive several noteworthy observations. In the context of comparing the various experiments, it can be noted that:

- All benchmarks for Layout3 exhibit symmetry around belt displacement n5. This symmetry arises because, as explained in paragraph 3.3.1, the two belts of the configuration move from bow to stern and vice versa, overlapping at n5 and exchanging places subsequently;
- The results for experiments Δq (Figure 6.2e) and Δr (Figure 6.2f) closely align with one another. It is a consequence of the airship's symmetry. The engine configurations do not favor rotations around $\mathrm{b}_{2\mathcal{B}}$ over $\mathrm{b}_{3\mathcal{B}}$;
- Engine configurations are optimized to facilitate control over pitch and yaw angles (Δq and Δr), while rotations around the roll angle (Δp) are notably more demanding to attain (Figure 6.2d in comparison to Figure 6.2e and Figure 6.2f);
- ΔU experiments (Figure 6.2e) are those that achieve better benchmarks, between one and two orders of magnitude lower than those of other experiments. This advantage is attributed to the main propeller, which significantly enhances control velocity along the $\mathrm{b}_{1\mathcal{B}}$ axis;
- Achieving velocity variations along the vertical $\mathrm{b}_{3\mathcal{B}}$ axis is more control expensive compared to variations along the lateral $\mathrm{b}_{2\mathcal{B}}$ axis (Figure 6.2b in comparison to Figure 6.2c);
- The experiment in which all states are perturbed simultaneously yields significantly inferior results (Figure 6.2g).

Analyzing the different configurations reveals the following trends:

- A consistent trend emerges, showing a gradual and general decline in the benchmark as the engines are positioned closer to the tail. The most favorable outcomes are achieved when the belts are located at n9. This trend can also be revealed graphically in the simulations presented in the paragraph 5.3.
- The configuration that performs best overall is Layout2-n9, which, in addition to the main propeller, has one belt with 8 ion thrusters mounted at the tail (-6m from CB).
- In the best performing belt displacement n9, Layout3 almost always performs like Layout1. Both these configurations share an identical aft belt with four ion engines. Layout3 distinguishes itself from Layout1 by an additional bow belt with four more ion engines. However, as it can be seen in Figure 6.1, even in the $\Delta(U, V, W, p, q, r)$ experiment, the one that requires more control effort, the bow engines are slightly utilized (ION5,ION6,ION7,ION8). It is therefore highlighted that, with reduced construction complexity, lower weight, and lower cost, Layout1 outperforms Layout3.

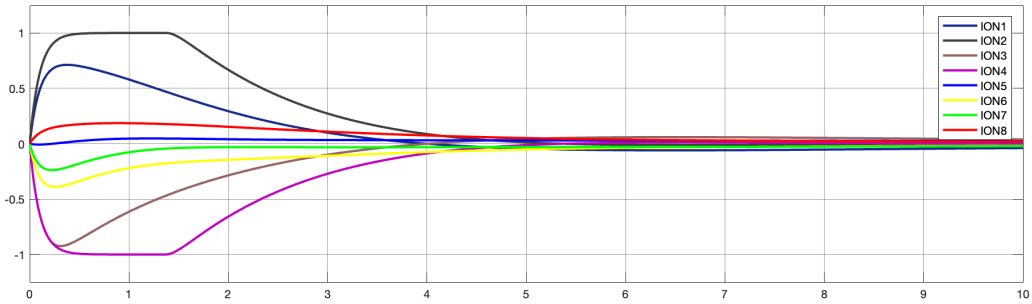

Figure 6.1: Layout3-n9, ION thrusters, $\Delta(U, V, W, p, q, r)$ experiment

- Both Layout1 and Layout2 exhibit superior performance when the motor belts are situated fully aft at n9. An exception arises in the first experiment (Figure 6.2e), in which they perform slightly better between n5 and n7. However, given that the ΔU experiment is carried out with greater simplicity, thanks to the main propeller, these variations are not considered significant. The performance differential between Layout1 and Layout2 remains consistent across all experiments, albeit not excessively pronounced.
- The highest overall performing configuration is Layout2-n9, featuring eight ion thrusters mounted at the tail, positioned 6 meters from the center of buoyancy (CB), in addition to the main propeller. However, it's worth noting that Layout1-n9 achieves very similar results while employing a significantly simpler structure. The introduction of a greater level of control discretization did not yield a substantial enhancement in control capabilities. In contrast, opting for a belt with four motors instead of eight leads to reductions in weight, construction costs, and overall complexity. The eight-engine configuration, on the over hand, does offer enhanced resilience in the event of an engine malfunction.

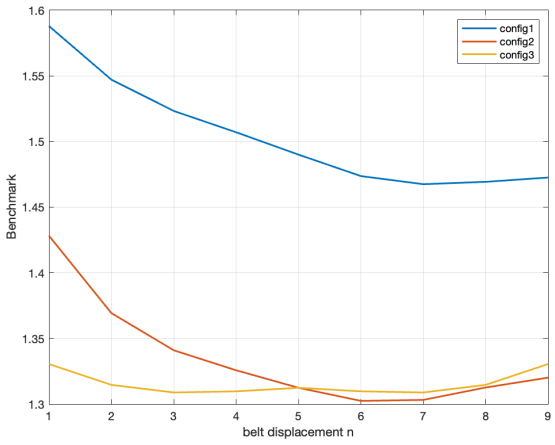

(a) ΔU experiments

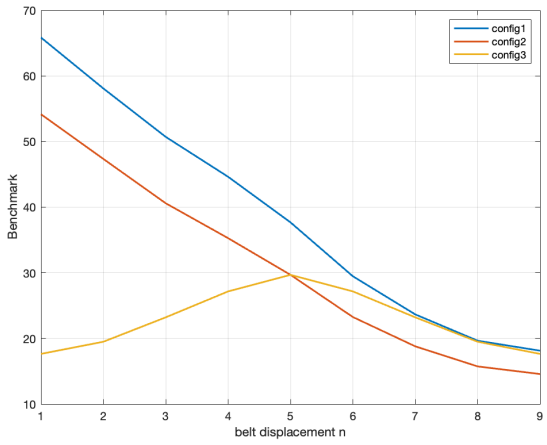

(b) ΔV experiments

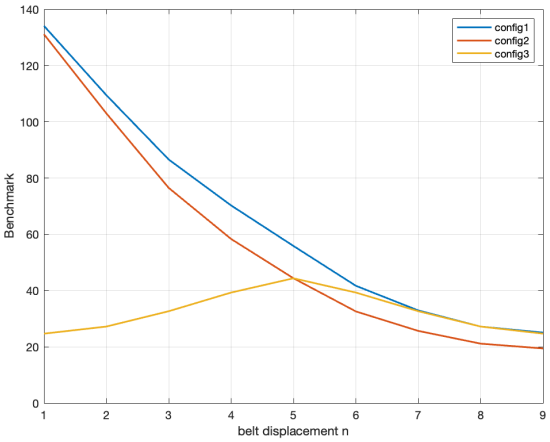

(c) ΔW experiments

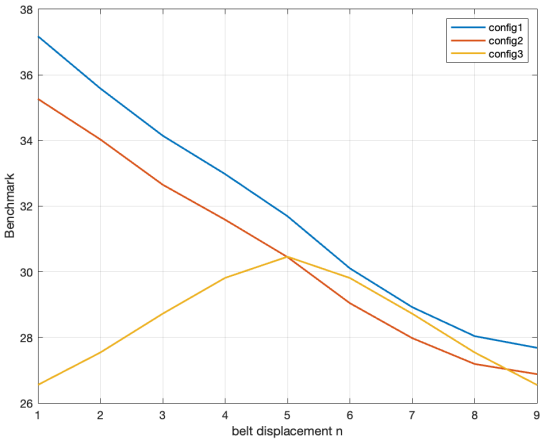

(d) Δp experiments

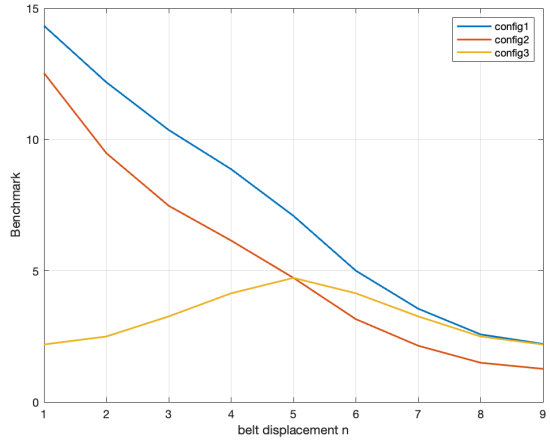

(e) Δq experiments

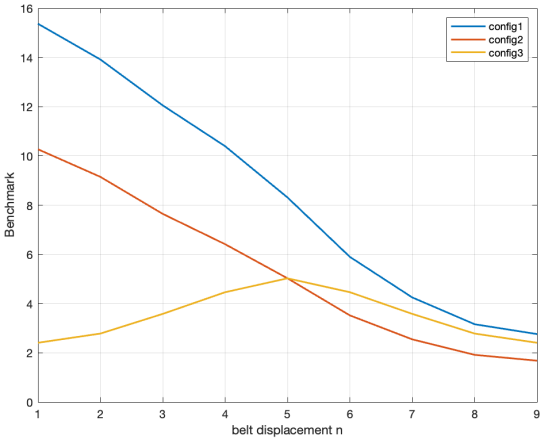

(f) Δr experiments

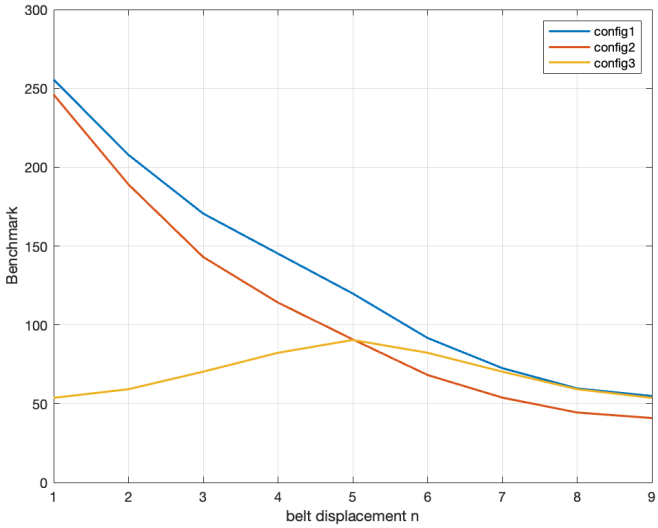

(g) $\Delta(U, V, W, p, q, r)$ experiments

Figure 6.2: Benchmark resoults

7. Conclusions

Airships technology will revolutionize airborne monitoring in the near future due to their flexibility, ease of transport and extended flight durations. This is evident through the numerous projects undertaken by major aviation companies, the emergence of innovative startups, and substantial institutional funding.

The primary objective of this master's thesis was to develop an analytical methodology for comparing various thruster layouts with a focus on dynamic control, evaluating the impact of motor positioning and quantity. Using established aeronautical principles, a comprehensive six-degree-of-freedom model was derived, explicitly formulating terms related to thrust characteristics. This model has been applied to a real case study utilizing the Lotte airship as baseline.

Diverse layouts were selected to highlight how thrust project design can influence controllability. To create a universally adaptable control strategy for all layouts, an LQR controller has been designed and tested. Ultimately, a significant benchmark was established to gauge how effectively different configurations resist disturbances. A series of experiments was then conducted for each configuration to assess its performance. The results, obtained in stable, horizontal, and trimmed flight conditions, clearly favor rear-mounted layouts. Furthermore, they reveal that pursuing greater directional control discretization does not yield significant improvements in responses.

Several promising directions for future research and development are worth considering. These include refining the models to account for previously overlooked factors like unsteady atmospheres, diverse flight conditions, and more comprehensive motor and aerodynamic modeling. Additionally, the exploration of alternative control inputs, such as tiltable electric motors or active control surfaces, could open up an interesting comparison of different types of control. Given the complex nature of the task, also influenced by the specific mission of the LTA and the external environment, a multitude of variables can be explored to identify the most optimal configuration.

References

[1] M. Belan, L. Arosti, R. Polatti, F. Maggi, S. Fiorini, and F. Sottovia. A paramet- ric study of electrodes geometries for atmospheric electrohydrodynamic propulsion. *Journal of Electrostatics*, 113(2):103616, 2021.

[2] Andrea Cecchi. Design and control of an air- ship moved by electrohydrodynamic propulsion. Master's thesis, Politecnico di Milano, 2021.

[3] M. V. Cook. *The Linearised Small Perturbations Equations of Motion for an Airship.* Cranfield Institute of Technology, 1990.

[4] S. Gomes and J. Ramos. Airship dynamic modeling for autonomous operations. *Technical report, IEEE International Conference on Robotics and Automation*, 1998.

[5] G. Khoury and D. Gillett. *Airship Technology.* Cambridge University Press, 1999.

[6] A. Kornienko. System identification approach for determining flight dynamical characteristics of an airship from flight data. *PhD thesis*, 2006.

[7] B. Kämpf. Flugmechanik und flugregelung von luftschiffen. *PhD thesis*, 2003.

[8] Y. Li, M. Nahon, and I. Sharf. Airship dynamics modeling: A literature review. *Progress in Aerospace Sciences*, 47, No. 3:pp. 217–239, 2011.

[9] Lalo Magni and Riccardo Scattolini. *Advanced and Multivariable Control.* Pitagora, 2014.

[10] K. Masuyama and S. R. Barrett. On the performance of electrohydrodynamic propul- sion. *Proceedings of the Royal Society A: Mathematical, Physical and Engineering Sciences*, 469, 2013.

[11] Marco Milanesi. Orientable thrust on airships: dynamics modeling and simulation. Master's thesis, Politecnico di Milano, DAER, 2021.

[12] Edoardo Mosca. *Optimal, Predictive and Adaptive Control.* Prentice Hall, 1995.

[13] J. B. Mueller, M. A. Paluszek, and Y. Zhao. Development of an aerodynamic model and control law design for a high altitude airship. *Technical report, Princeton Satellite Systems*, 2012.

[14] R. C. Nelson. *Flight stability and automatic control.* WCB/McGraw Hill, 1998.

[15] B.N. Pamadi. *Performance, Stability, Dynamics, and Control of Airplanes, AIAA Education Series.* AIAA Education Series; American Institute of Aeronautics and Astronautics, Inc.: Reston, VA, USA, 2004.

[16] Carlo E. D. Riboldi. On the optimal tuning of individual pitch control for horizontal-axis wind turbines. *Wind Engineering*, 40:398, 2022.

[17] Carlo E. D. Riboldi and Alberto Rolando. Layout analysis and optimization of airships with thrust-based stability augmentation. *Aerospace*, 9:393, 2022.

[18] Jones S.P and DeLaurier J.D. Aerodynamic estimation techniques for aerostats and airships. *J. Aircraft*, 20(2):120–126, 1982. An optional note.

[19] Sottovia F. (+ superv. F. Maggi). Design and testing of a laboratory setup for ehd propulsion studies. Master's thesis, Politecnico di Milano, DAER, 2020.

[20] P. Valsecchi. Ingegneria e progettazione del dirigibile : analisi storica e prospettive future. *PhD thesis*, 2019.

Abstract in lingua italiana

I dirigibili, una tecnologia pionieristica quasi un secolo fa, stanno vivendo un rinnovato interesse di ricerca grazie alla loro capacità di volare a lungo con un consumo minimo di carburante. Questa tesi si inserisce nella ricerca di nuove tecniche di propulsione e controllo. Il controllo dinamico dei dirigibili è sempre stato una delle sfida maggiori da affrontare. Per aumentare la controllabilità sono state esplorate diverse soluzioni dal mondo nautico, come i propulsori di prua e i motori orientabili. Purtroppo implementare queste tecnologie in un velivolo LTA aumenta notevolmente i pesi e la complessità della costruzione. Alla luce del crescente interesse per i dirigibili ad alta quota (HAA) e per il volo autonomo, un obiettivo importante è quello di semplificare i progetti mantenendo le prestazioni richieste.

Questa ricerca esplora il controllo dei dirigibili utilizzando cinture di propulsori fissi. Vengono utilizzate diverse configurazioni di propulsori elettro-idrodinamici (EHD). I motori EHD utilizzano forze elettrostatiche per generare spinta attraverso l'accelerazione degli ioni. Se si dimostreranno efficaci, queste tecnologie potrebbero ridurre la necessità di avere strutture mobili e complesse come le superfici di controllo o i motori orientabili.

L'obiettivo primario di questa tesi è analizzare come questi propulsori possano essere posizionati strategicamente per ottimizzare la reiezione dei disturbi. Lo studio mira a sviluppare uno strumento analitico per confrontare diversi layout di motori in termini di controllo dinamico, valutando gli effetti della quantità di motori e del loro posizionamento. La metodologia di ricerca prevede la derivazione di un modello dinamico dalla letteratura esistente e adattarlo per incorporare gli input delle cinture di motori ionici. La validazione del modello linearizzato è ottenuta attraverso un'analisi agli autovalori, confrontando i risultati con la letteratura esistente. Viene sviluppata una strategia di controllo LQR multivariabile per affrontare i disturbi nelle varie configurazioni. Le simulazioni numeriche valutano la capacità di ciascun layout di riportare all'equilibrio gli stati perturbati, con un benchmark definito per valutare le prestazioni.

Lo studio si conclude presentando i risultati completi dei test numerici, offrendo approfondimenti sull'influenza dei parametri di progettazione sulle prestazioni e discutendo le caratteristiche di un layout ottimale.

Parole chiave: Dirigibili, LTA, Controllo dirigibile, LQR, Spinta Distribuita, Motori Ionici

Ringraziamenti

Questo spazio è dedicato a tutte le persone con cui ho condiviso le fortissime emozioni vissute durante i miei studi universitari.

Vorrei innanzitutto ringraziare il mio relatore prof. Carlo Riboldi, che mi ha dato la libertà di ricercare in un ambito di mio grande interesse, e che con la sua infinita disponibilità mi ha seguito in ogni passo della ricerca.

Un grande ringraziamento va ai miei genitori, che hanno sempre cercato di supportarmi, spingermi e motivarmi perché arrivassi a questo importante traguardo. Ai miei fratelli, con i quali ho condiviso gran parte della mia crescita, e ai miei nonni, che per me sono stati dei secondi genitori. Grazie per avermi invitato sempre al massimo impegno, per avermi incoraggiato nei momenti difficili. Spero di avervi reso orgogliosi.

Un ringraziamento dal profondo del cuore a Maria, compagna di avventure e supporter numero uno.

Un ringraziamento grande come un abbraccio, e anche di più, agli amici di una vita Ale, Cume, Carret, Manzo, Manu, Steven e Stein. In ogni momento fuori e ad ogni ritorno a casa loro erano presenti. Un ringraziamento anche a tutti gli amici che ho conosciuto in questo lungo percorso, in particolare ad Andrea, Andrea, Giulia, e Giacomo, con cui ho anche avuto l'onore di cominciare l'avventura di FloFleet. Senza le stancanti, ma soddisfacenti, maratone di studio insieme probabilmente non avrei combinato granchè.

Un ringraziamento a tutte le persone che lavorano, hanno collaborato e collaboreranno a Flofleet, perché questa tesi possa essere un tassello nella realizzazione di qualcosa di più grande.